



Water adsorption on SrTiO₃(001): II. Water, water, everywhere

A.E. Becerra-Toledo ^{a,*}, J.A. Enterkin ^{b,1}, D.M. Kienzle ^a, L.D. Marks ^a

^a Department of Materials Science and Engineering, Northwestern University, Evanston, IL 60208, USA

^b Department of Chemistry, Northwestern University, Evanston, IL 60208, USA

ARTICLE INFO

Article history:

Received 28 July 2011

Accepted 11 January 2012

Available online 17 January 2012

Keywords:

Strontium titanate

Density functional theory

Water adsorption

Surface reconstruction

X-ray photoelectron spectroscopy

Oxide surfaces

ABSTRACT

The role of water adsorption on Ti-rich SrTiO₃(001) surface reconstructions is studied. Density functional calculations with hybrid functionals of numerous adsorption configurations indicate that the relative stability of the different reconstructions is strongly altered by the addition of water, with all the reconstructions having comparable energy for half-monolayer coverage, most with a fair degree of hydrogen bonding. This strongly suggests that which reconstruction is observed depends upon a competition between the kinetics of ordering and dehydration. X-ray photoelectron spectra are consistent with the theoretical predictions for the dehydration of the 2 × 1 and c(4 × 2) reconstructions.

© 2012 Elsevier B.V. All rights reserved.

1. Introduction

The present manuscript is the second of two papers dealing with reconstructions on the strontium titanate (001) surface and the effects of water chemisorption. In Part I we examined the scanning tunneling images of the 2 × 1 and c(4 × 4) surfaces, demonstrating that the images are most consistent with dehydration of an initially hydrated 2 × 1 surface rather than a dry 2 × 1 structural model, as previously assumed.

In this paper we consider water adsorption on the other SrTiO₃(001) reconstructions with the same surface excess of TiO₂, namely the c(4 × 2), 2 × 2 and (√2 × √2)R45° (“RT2” hereafter), in addition to the 2 × 1. We focus primarily on the ab-initio energetics, with supporting evidence from in-situ annealing experiments and X-ray photoelectron spectroscopy (XPS) measurements. We find that all the reconstructions can adsorb water at ambient temperature and pressure, and the energies of the different reconstructions are almost degenerate for half-monolayer water coverage. These results are consistent with strong water chemisorption on defective surfaces formed either by ion-beam milling or cleavage, with relatively sluggish dehydration kinetics. Which reconstruction forms is therefore an issue of kinetics, not just thermodynamics.

The topic of water interaction with strontium titanate surfaces has already merited exploration in numerous reports, since SrTiO₃ is a simple model system for perovskite oxides, and for ionic systems with

mixed cation valence states in general. It is itself a promising material for several practical applications, including photocatalytic water-splitting [1,2], as an anode material in Li-ion batteries [3] and as a catalytic support [4,5]. Experimentally, the consensus in the literature is that water adsorbs molecularly (i.e. non-dissociatively) on unreconstructed surfaces [6], whereas dissociative adsorption occurs strongly on defective surfaces, be it at O vacancy sites [6,7] or steps [8].

On the theoretical front, Wang et al. [9] provided a simple geometrical model for the full-monolayer (in this manuscript, 1 ML = 1 molecule per 1 × 1 surface cell) molecular H₂O adsorption on a TiO₂-truncated SrTiO₃(001) surface and used density functional theory (DFT) to predict the adsorption energy and bond lengths. Evarestov et al. [10] took the next step by using a hybrid Hartree–Fock/DFT approach to study the adsorption of water on bulk-like (001) TiO₂ and SrO truncations, allowing for both dissociative and molecular adsorption models; both 1 and 2 ML water adsorption were considered. On the TiO₂-terminated surface at full-monolayer coverage, the molecular configuration was indeed found to be more stable than the dissociative mode, in agreement with experimental observations. Adsorption energies and bond lengths were also reported. Recently, Hinojosa et al. [11] revisited the topic of dissociative and molecular H₂O adsorption on bulk-like TiO₂ and SrO truncations, now examining water coverage of 1 ML and below, again via DFT computations. The 1 ML results on the Ti-rich surface largely agree with Evarestov et al. regarding both geometry and relative energies; however, the dissociative configuration is predicted to be more stable on the TiO₂ termination at a H₂O surface coverage of 0.5 ML or less, in apparent contradiction with experiment.

It bears noting that bulk-like depictions of surfaces are often unrealistic, since oxide surfaces tend to stabilize by reconstructing.

* Corresponding author. Tel.: +1 847 491 7809; fax: +1 847 481 7820.

E-mail address: andres@u.northwestern.edu (A.E. Becerra-Toledo).

¹ Present address: Chemical Sciences and Engineering Division, Argonne National Laboratory, Argonne, IL 60439, USA.

Therefore, the usefulness of assuming bulk-like truncation geometries is questionable. To date, the theoretical modeling of water adsorption on reconstructed oxide surfaces has been reported in very few studies [12–14]. The most systematic reports focused on the reconstructions in rocksalt MgO/NiO(111) surfaces [12,14]; supported by XPS and transmission electron diffraction (TED) data, DFT calculations revealed the crucial role played by H₂O in the formation of (and transition between) different surface structures.

The SrTiO₃(001) orientation provides us with several experimentally-observed periodic reconstructions of known structure, on which water adsorption may be modeled. These include the aforementioned 2 × 1 surface [15], as well as the “zigzag” 2 × 2 [16] and c(4 × 2) [17] structures. All of these share the distinguishing feature that they terminate in two TiO₂ atomic layers. Moreover, a conundrum exists at present: a theoretical study of possible double-TiO₂-layer structures [18] calculated that the RT2 reconstruction should have the lowest surface energy, whereas the known 2 × 1 structure is of relatively high energy. However, the RT2 surface has never been observed. The present study of H₂O adsorption on reconstructed SrTiO₃(001) surfaces resolves this apparent contradiction.

The structure of this paper is as follows. We begin by testing our computational method with simple adsorption cases previously modeled in the literature. 0 ML, 0.5 ML, and 1 ML water adsorption coverages are then examined for the four different surface periodicities via DFT calculations and chemical bonding analysis. A full thermodynamic picture is built for these and the hydrated c(4 × 4) reconstruction, described in Part I. Complementary TED patterns and XPS spectra of reconstructed single-crystal surfaces are shown in support of the calculations. We then conclude with a brief discussion.

2. Methods

2.1. Theoretical

2.1.1. Density functional theory

Density functional calculations were performed to model all surfaces, using the periodic slab configuration. The DFT calculations were carried out with the full-electron-potential WIEN2k code [19] with an augmented plane wave + local orbital (APW + lo) basis set. Every structure considered was allowed to relax such that the residual force on each atom was below 0.1 eV/Å. Every bare surface slab consisted of 13 atomic layers, i.e. a double TiO₂ layer termination on each side with five bulk SrTiO₃ as the slab core; surfaces with adsorbed water used this same base structure. Muffin-tin radii of 2.36, 1.70, 1.20 and 0.60 bohr were used for Sr, Ti, O and H, respectively. A *k*-point mesh equivalent to a 6 × 6 × 6 mesh for a bulk SrTiO₃ unit cell was used, as well as a *K*_{max} of 5.5/1.2 bohr⁻¹. The SrTiO₃ bulk lattice parameter was optimized and a value of 3.893 Å was used throughout, in good agreement with the experimental value of 3.905 Å.

The exchange-correlation functional of choice was the PBEsol-Hybrid [20] implementation of the generalized gradient approximation, with exact exchange fraction of 0.5 for the Ti-d levels. The amount of exact exchange was optimized to match experimental atomization energies of TiO_x molecules, as done for other studies [12,21]; see Appendix A for more details. The PBEsol functional is known to yield good lattice constants and surface energies, but poor atomization and adsorption energies [22]. In order to address this, the final energy numbers were obtained via an on-site implementation of the revTPSS functional, which significantly corrects the shortcomings of PBEsol with little downside [23]; the conventional term for revTPSS with exact-exchange corrections is revTPSSh.

Surface energies at *T* = 0 K were calculated and normalized as

$$E_{\text{surf}/1 \times 1}^0 = (E_{\text{slab}} - n_{\text{STO}}E_{\text{STO}} - n_{\text{TiO}_2}E_{\text{TO}} - n_{\text{w}}E_{\text{w}}) / 2N_{1 \times 1},$$

where *n*_{STO} is the equivalent number of SrTiO₃ bulk unit cells in the slab, *n*_{TO} is the equivalent number of TiO₂ bulk unit cells, *n*_w is the number of equivalent water molecules adsorbed per slab, *N*_{1 × 1} is the number of 1 × 1 surface cells, *E*_{STO} is the energy of a bulk SrTiO₃ unit cell, *E*_{TO} is the energy of a bulk rutile TiO₂ unit cell and *E*_w is the energy of an isolated H₂O molecule. An error estimate of 0.05 eV/1 × 1 cell was used for the hybrid revTPSSh surface energy values, as explained in Appendix A.

Adsorption energies per water molecule were computed as

$$E_{\text{ads}} = (E_{\text{dry}} + n_{\text{w}}E_{\text{w}} - E_{\text{wet}}) / n_{\text{w}},$$

where the subscripts *E*_{dry} and *E*_{wet} are the slab energies for the bare surface and the relevant hydrated model.

The surface energies were also computed as a function of temperature, by including a correction for the chemical potential of water in its gaseous phase. This was done as

$$E_{\text{surf}/1 \times 1}(T, P) = E_{\text{surf}/1 \times 1}^0 - (n_{\text{w}} / 2N_{1 \times 1}) \Delta \mu_{\text{w}}^{0, K \rightarrow T},$$

where

$$\mu_{\text{w}}(T, P) = \mu_0 - (T - T_0)S(T) + RT \ln(P/P_0).$$

Here, the zero subscript corresponds to standard temperature and pressure. The entropy *S*(*T*) was obtained from Ref. [24] and we assume a partial pressure of water of 0.02 atm, which is typical for 50% relative humidity at room temperature. With such a method we are assuming that the phonon entropy of the different surfaces is very similar and cancel to first order and, since all the models considered are insulating, there is no electronic entropy contribution. This is a reasonable approximation, as suggested by earlier calculations (see, for example, Ref. [25]).

2.1.2. Bond valence sum analysis

For a given ion, the bond valence sum (defined to be positive for cations and negative for anions) is calculated as:

$$\text{BVS} = \pm \sum_i \text{BV}_i,$$

a sum over all bonds of the individual bond valences, defined as,

$$\text{BV} = \exp((R_0 - R)/b),$$

where *R* is the bond length, *R*₀ is an experimentally-determined standard bond distance for the particular ion pair in question, and *b* is an empirical constant, typically 0.37 Å. The following *R*₀ values were consistently employed: 2.118 Å for Sr²⁺ – O²⁻, 1.815 Å for Ti⁴⁺ – O²⁻ [26] and 0.957 Å for H⁺ – O²⁻. The latter was set to the O – H distance in gaseous H₂O [27]. The volume of each supercell was expanded isotropically to match the lattice parameter to the experimental SrTiO₃ lattice parameter of 3.905 Å. The bond valence sums were computed using the KDist software from the Kalvados program suite [28].

A useful metric in bulk inorganic structures is the global instability index (GII), so named by Salinas-Sánchez et al. [29]. This is simply the root mean square average, over all atoms, of the deviation of the bond valence sum from the idealized formal valence, *BVS*₀:

$$\text{GII} = \left(\overline{(\text{BVS} - \text{BVS}_0)^2} \right)^{1/2}.$$

Typically, stable room-temperature bulk structures have a GII below 0.2 valence units [30]. By analogy to the GII, we use the surface instability index (SII), a figure of merit for relaxed surfaces introduced by Enterkin et al. [31]. The SII is calculated in the same way as its bulk

counterpart, but only taking into account the atoms in the topmost two layers, plus any adsorbed atoms. The choice of DFT exchange–correlation functional proves to be significant for obtaining accurate BVS values, as examined in Appendix B.

2.2. Experimental

Single-crystal (100)-oriented SrTiO₃ wafers (10×10×0.5 mm, 99.95% purity, one side epi-polished) were commercially purchased from MTI Corporation (Richmond, CA). 3 mm-diameter discs were cut from each wafer using a Gatan 360 rotary disc cutter and a SiC slurry. Each disc was subsequently thinned to obtain a self-supporting transmission electron microscopy sample: first, each disc was mechanically thinned to ~100 μm thickness with abrasive SiC paper; then, its center was dimpled with a Gatan dimple grinder and a diamond slurry to ~25 μm thick; finally, the sample was ion milled with a Gatan Precision Ion Polishing System to electron transparency with 2.5–6.0 keV Ar⁺ ions at glancing incidence angle (<3°).

In order to remove implanted ions and other impurities, the specimens were washed for several seconds in a concentrated HCl:HNO₃ (equal parts by volume) solution. After several rinsing cycles with deionized water and drying, samples were annealed in air to repair the damage and the preferential removal of light atoms such as O. Each sample was placed in an alumina boat in a fused silica tube, which was inserted into a Carbolite STF 15/51/180 furnace and heated to 850–950 °C; this temperature range was selected to target the formation of the 2×1 and c(4×2) reconstructions, following literature [32].

Samples were mounted in a custom-made alumina ring and secured with a tungsten spring clip, then introduced into the ultra high vacuum (UHV) SPEAR (Specimen Preparation, Evaluation, Analysis and Reaction) system at Northwestern University, which is interfaced with a UHV Hitachi H9000 transmission electron microscope (TEM) with base pressure of 1×10⁻¹⁰ Torr. After insertion into the SPEAR load lock chamber, this compartment was pumped down and wrapped with a thermal blanket filled with dry ice to act as a cold trap to help the chamber reach UHV conditions. Once inside the system, samples were transported, always in vacuo, between different compartments: the gas treatment cell, for anneals with a resistive heating stage; the analytical chamber, for electron-gun anneals or XPS analysis; and the TEM, for electron diffraction and real space imaging. No further exposure to air took place, unless otherwise stated.

XPS was carried out with an Al K_α source using a PHI model 05-458 hemispherical analyzer. Spectra were normalized and corrected for charging effects with the known SrTiO₃ Ti-2p_{3/2} peak with binding energy of 458.8 eV. The Sr-3d, Ti-2p, O-1s and C-1s regions of interest were scanned in detail (0.1 eV step size, 0.5–0.655 s dwell time, averaged over 5–25 scans), after a broad survey scan. Each peak was fit to a Gaussian curve, with the background signal subtracted linearly. The appearance of a high binding energy shoulder on the O-1s peak, which may indicate hydroxyl-type bonding, was monitored and quantified. [33–36]. It is known that Ti³⁺ also leads to a similar shoulder feature, as it does in rutile TiO₂ [34,35]; therefore, the presence of Ti³⁺ was simultaneously tested by looking for a low binding energy shoulder on the Ti-2p_{3/2} peak.

Electron-gun annealing was performed with a Kimball Physics EMG-14 gun. The sample was bombarded with a low-energy beam (accelerating voltage of 4.28 kV) and temperature was increased by either increasing the filament current, or by focusing the beam onto the central, thinner area of the sample, which is the region analyzed by TEM. The temperature was measured with an infrared optical pyrometer. Two main concerns exist with this type of heating. First, while high temperatures are attainable, the required beam size is significantly smaller than the sample diameter, resulting in inhomogeneous heating. Second, low-energy electron bombardment is known to reduce titanium in rutile TiO₂ [37]; this was found to occur with

SrTiO₃ even in an oxygen gas environment. Conversely, annealing with a resistive heating stage resulted in uniform heating, but the maximum achievable temperature was lower than with the electron gun. In the latter setup, a calibrated thermocouple was employed to monitor the temperature.

3. Results

3.1. Theoretical

From a computational stance, the main new results relate to the adsorption of H₂O on known TiO₂-rich SrTiO₃(001) surface reconstructions. In order to test the reliability of our computational method, we modeled the full-monolayer water adsorption on the bulk-like SrTiO₃(001) TiO₂-truncation, both in the dissociative and molecular modes. This enables a direct comparison to three previous theoretical reports [9–11]. Qualitatively, the relaxed dissociative and molecular structures are very similar to those previously examined. The molecularly-adsorbed water molecule, seen in Fig. 1(a), orients itself so as to generate a rough in-plane alignment of its O–H bonds with oxygen atoms at the surface. In the dissociative adsorption case, the adsorbed OH and the lone H adsorbed on a surface O tilt slightly in opposite directions. The relaxed structures are available as supplementary material in the Crystallographic Information File (CIF) format.

Several characteristic interatomic distances in these structures, as well as adsorption energies, are tabulated in Table 1. As in the previous studies, we found that the surface with molecularly adsorbed water is more stable than the dissociative case for water coverage of one molecule per 1×1 cell. The only significant discrepancy is found in the molecular adsorption case, where the H₂O molecule tilts more than previously predicted: one of the hydrogen atoms (H2) comes closer to – while the other (H1) goes farther from – the surface than in the other calculations. Otherwise, the predictions agree very well with results in the literature, especially with those from the recent Hinojosa et al. [11] report.

We will now examine in more detail the 2×1, RT2, 2×2 and c(4×2) double-layer (DL) TiO₂ reconstructions. For each case, additional structures with 0.5 and 1 ML H₂O adsorption are explored; please

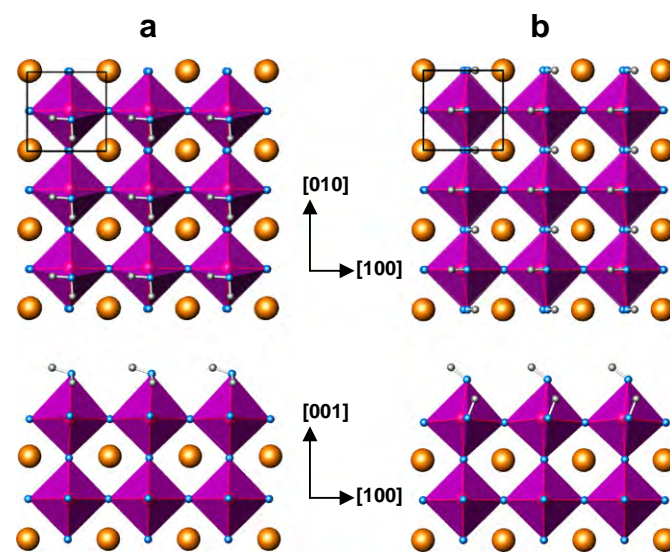


Fig. 1. Polyhedral representation of the full-monolayer water adsorption configurations on the TiO₂-truncated SrTiO₃(001) surface: (a) molecular and (b) dissociative modes. Plan view on top and profile view at the bottom. Surface cells outlined. Sr = large orange, Ti = red, O = blue, and H = gray. Ti-centered 6-fold coordination polyhedra are purple.

Table 1

Calculated interatomic distances (in Å) and adsorption energies (in eV/molecule) for the water adsorption structures on the bulk-like TiO₂-terminated SrTiO₃(001) surface. The *mol* and *diss* superscripts refer to the relaxed molecular and dissociative adsorption configurations, respectively.

	Wang et al. [9]	Evarestov et al. [10]	Hinojosa et al. [11]	This work
Ti–O _w ^{mol}	2.23	2.27	2.27	2.24
H1–O1 ^{mol}	2.59	–	2.42	2.75
H2–O2 ^{mol}	2.23	1.85	1.82	1.73
O _w –H1 ^{mol}	0.984	–	0.98	0.981
O _w –H2 ^{mol}	0.986	–	1.00	1.02
Ti–O _w ^{diss}	–	1.88	1.90	1.90
E _{ads} ^{mol}	0.83	0.87	0.79	0.80
E _{ads} ^{diss}	–	0.77	0.59	0.58

note that 1 ML is defined differently than in the previous studies [10,11]. It must be emphasized that the number of possible geometric configurations is prohibitively large. Therefore, the set of structures studied herein is not an exhaustive list and it is certainly possible that other structures of the same stoichiometry are of lower surface energy. However, we aim to tackle the most likely low-energy candidate structures, as dictated by chemical intuition and reasoning, making use of bond-valence analysis of the dry structures to screen out many adsorption configurations.

Bond valence sums are calculated for the lowest-energy structure of each periodicity and water coverage; these structural models are ultimately used for further thermodynamic analysis.

3.1.1. The 2×1 surface

The 2×1 reconstruction was structurally solved by Erdman et al. [15] using a combination of TED, direct methods and DFT. It exhibits a characteristic “dangling” oxygen (in single coordination, O1 in Table 2) and one mirror plane. As can be seen in its polyhedral representation in Fig. 2(a), this reconstruction shows parallel zigzagging rows of surface polyhedra.

As can be seen in Table 2, several top-layer atoms in the dry 2×1 reconstruction are very undercoordinated, including both Ti and the “floating” O (those which are not bound to subsurface Ti, borrowing the nomenclature by Warschkow et al. [18]). These drive the

Table 2

Bond valence sums for the near-surface atoms of the 2×1 dry structure and low-energy hydrated models. *m* is the atom multiplicity per 1×1 cell. The SII is also shown for each surface. For the hydrated models, the SII shown in parenthesis is calculated without taking the adsorbed atoms into account.

	2×1			2×1DissA			2×1SatB		
	Atom	<i>m</i>	BVS	Atom	<i>m</i>	BVS	Atom	<i>m</i>	BVS
ML H ₂ O	0			0.5			1		
SII	0.28			0.10 (0.11)			0.12 (0.14)		
Adsorbed atoms				O _w 1	0.5	−1.93	O _w 1	0.5	−1.96
				H1	0.5	0.96	H1	0.5	0.97
				H2	0.5	0.95	H2	0.5	1.04
							O _w 2	0.5	−1.84
							H3	0.5	0.96
							H4	0.5	1.01
Top layer	Ti1	0.5	3.64	Ti1	0.5	3.95	Ti1	0.5	3.90
	Ti2	0.5	3.45	Ti2	0.5	3.83	Ti2	0.5	3.89
	O1	0.5	−1.54	O1	0.5	−1.97	O1	0.5	−1.95
	O2	0.5	−1.68	O2	0.5	−2.04	O2	0.5	−1.92
	O3	0.5	−2.20	O3	0.5	−2.06	O3	0.5	−2.12
	O4	0.5	−1.88	O4	0.5	−1.88	O4	0.5	−2.30
2nd layer	Ti3	0.5	4.01	Ti3	0.5	3.93	Ti3	0.5	4.00
	Ti4	0.5	4.15	Ti4	0.5	4.04	Ti4	0.5	3.90
	O5	0.5	−2.05	O5	0.5	−1.80	O5	0.5	−1.82
	O6	0.5	−1.91	O6	0.5	−2.08	O6	0.5	−1.83
	O7	0.5	−1.95	O7	0.5	−2.01	O7	0.5	−1.99
	O8	0.5	−2.31	O8	0.5	−2.17	O8	0.5	−2.13

relatively large SII, which correlates with the high surface energy; both of which are unusual for an experimentally observed structure.

Several half-monolayer configurations (1 H₂O per 2×1 cell) were modeled:

2×1Mol: In the dry case, it is clear that of the two surface Ti, atom Ti2 is more exposed (and more undercoordinated, as seen in Table 2); therefore, Ti2 is the natural choice for the adsorption site of molecular water. Much like the full-monolayer molecular adsorption on bulk-like TiO₂, the O–H bonds align with surface O atoms (in this case, O2 and O4). This structural model, however, is unstable – its surface energy is 0.37 eV/1×1 higher than the following case.

2×1DissA: Dissociative adsorption, where an OH group adsorbs to the aforementioned Ti2 site. The remaining H binds to the dangling O1 atom, previously in single coordination. This preserves the original mirror plane and is the lowest energy structure among half-monolayer “wet” 2×1 surfaces. This structure is displayed in Fig. 2(b).

2×1DissB: Dissociative adsorption, similar to 2×1DissA, except for the adsorption of the lone H on O2, which is the second most undercoordinated anion. This is also unstable, 0.59 eV/1×1 higher in energy than 2×1DissA.

Model 2×1DissA provides a very low SII (Table 2), a result of the almost ideal BVS of the surface atoms.

Two full-monolayer cases of 2×1 periodicity were studied:

2×1SatA: Double dissociative adsorption. Similar to 2×1DissA, this structure adds an OH group to the previously shielded Ti1 atom, while the other lone H binds to O2. This renders all Ti 6-fold coordinated and forces the distinctive titanyl bond from the dry structure to be parallel to the surface. It is worth noting that the mirror plane is also preserved here even when no symmetry constraint is applied, and that upon relaxation all four O–H bonds lean in the same direction.

2×1SatB: Double dissociative adsorption. Similar to 2×1SatA, except that the second lone H binds not to O2, but to O4, which was the most underbonded surface oxygen. This new O–H leans in the direction opposite to all the others, as shown in Fig. 2(c). This structure was found to be more stable than 2×1SatA by 0.24 eV/1×1.

With the exception of O4, which is now overcoordinated, the BVS remain near the expected values (Table 2). The SII of 2×1SatB, while slightly higher than for the half-monolayer case, is significantly lower than for the bare 2×1.

3.1.2. The RT2 surface

The RT2 reconstruction was the lowest energy structure among all DL structures proposed by Warschkow et al. [18]. However, this surface has never been observed experimentally. It has p2gg symmetry and, as seen in Fig. 3(a), it consists of parallel rows of surface polyhedra running along a <110>-type direction.

Table 3 shows that the BVS are mostly reasonable and the SII of the RT2 is better than for all other dry DL reconstructions. While some of the surface atoms are somewhat undercoordinated, their divergence from the expected BVS is relatively small.

Two 0.5 ML structures (1 H₂O per RT2 cell) were examined:

RT2Mol: Since all surface Ti are equivalent in the dry structure, the adsorption site for molecular H₂O is arbitrary. The new Ti–O bond tilts so as to favor a rough alignment of each of the O–H bonds toward a neighboring O2 atom. The O2 have lower coordination than O1 since they are not bound to a Ti beneath and hence they lift up slightly. This structure was examined with no in-plane symmetry.

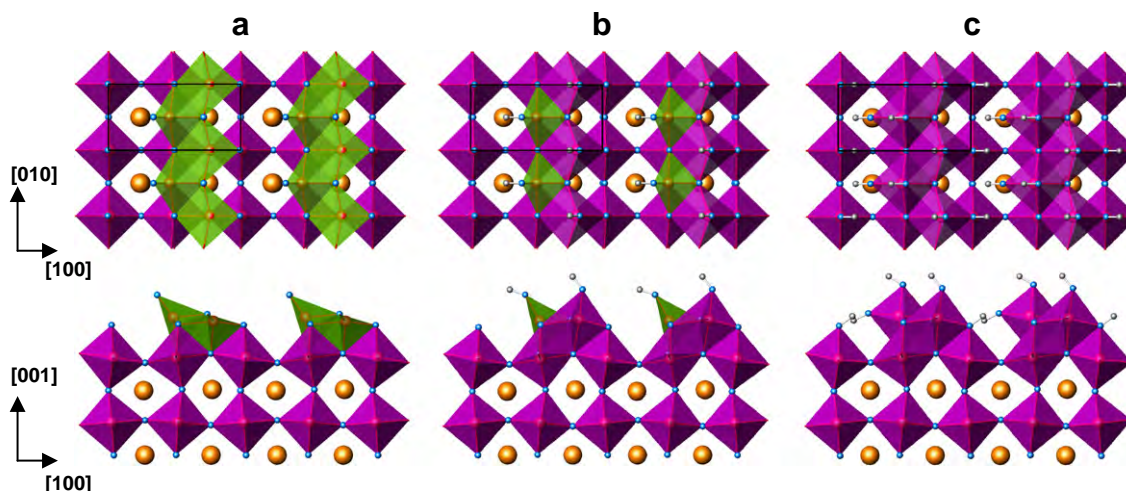


Fig. 2. Polyhedral representation of (a) the bare 2×1 surface, (b) the half-monolayer 2×1 DissA model, and (c) the full-monolayer 2×1 SatB model: plan view (top) and profile view (bottom). Surface cells outlined. Ti-centered 5-fold coordination polyhedra are green; legend follows Fig. 1 otherwise.

RT2Diss: Dissociative adsorption, where an OH group binds to an arbitrary surface Ti, with the O–H bond tilting toward one of the neighboring O2 atoms (O2b in Table 3). The extra lone H binds to the other O2 (O2a), and this new O–H bond points toward an O1 atom (O1b) from the next diagonal row of surface polyhedra so as to form an H-bond (2.07 \AA), as can be seen in Fig. 3(b). Like in the previous case, no in-plane symmetry was enforced. Although the difference is within error, this structure is calculated to be lower in energy by $0.03 \text{ eV}/1 \times 1$.

Two full-monolayer structures with RT2 periodicity were modeled:

RT2SatD: Double dissociative adsorption. A hydroxyl group binds to each surface Ti. Upon relaxation, all these O–H bonds roughly align in-plane, leaning toward the same $\langle 110 \rangle$ -type direction. Each lone H binds to an O2 atom; as in RT2Diss, each new O–H bond points toward an O1 from the next row of surface polyhedra, forming an H-bond ($\text{H}_2\text{--O1b} = 1.85 \text{ \AA}$; $\text{H}_3\text{--O1a} = 1.86 \text{ \AA}$). This structure is shown in Fig. 3(c).

RT2SatM: Double molecular adsorption. A water molecule adsorbs on each surface Ti site. No in-plane symmetry enforced. Each O–H bond originally points toward a nearby O2, but this is no longer true upon relaxation. This structure is found to be $0.28 \text{ eV}/1 \times 1$ higher in energy than RT2SatD.

Model RT2Diss largely corrects the BVS shortcomings of the bare RT2 surface. However, it does leave the top-surface O2a and the sub-surface O4a atoms overcoordinated. Meanwhile, RT2SatD does the same to top-surface Ti and all O2-type atoms. Neither hydrated model has comparably better metrics than the dry RT2 structure.

3.1.3. The “zigzag” 2×2 surface

Also proposed by Warschkow et al. [18], this geometry was found in their report to be the most stable DL structure with 2×2 periodicity. It was also observed to coexist with the 2×1 reconstruction by Herger et al. via surface X-ray diffraction [16]. This surface has $p2gm$ symmetry and can be qualitatively described as an ordered alternation of 2×1 units. As can be seen in Fig. 4(a), the 2×2 structure also yields a zigzagging row of surface polyhedra.

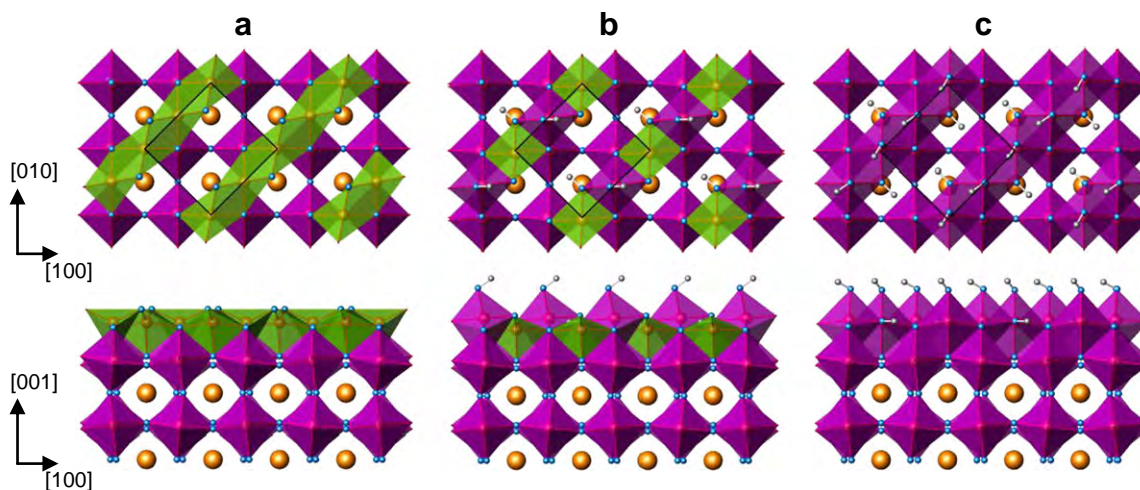


Fig. 3. Polyhedral representation of (a) the bare RT2 surface, (b) the half-monolayer RT2Diss model, and (c) the full-monolayer RT2SatD model: plan view (top) and profile view (bottom). Surface cells outlined.

Table 3
Bond valence sums for the near-surface atoms of the RT2 dry structure and low-energy hydrated models. The SII is also shown for each surface.

	RT2			RT2Diss			RT2SatD		
ML H ₂ O	0			0.5			1		
SII	0.13			0.14 (0.15)			0.13 (0.15)		
	Atom	m	BVS	Atom	m	BVS	Atom	m	BVS
Adsorbed atoms				O _w	0.5	-1.87	O _w 1	0.5	-1.90
				H1	0.5	0.95	H1	0.5	0.99
							H2	0.5	1.00
							O _w 2	0.5	-1.89
Top layer				H3	0.5	1.01	H3	0.5	1.01
				H4	0.5	0.97	H4	0.5	0.97
	Ti1	1	3.82	Ti1a	0.5	4.04	Ti1a	0.5	4.17
				Ti1b	0.5	3.90	Ti1b	0.5	4.14
	O1	1	-2.04	O1a	0.5	-2.01	O1a	0.5	-2.03
				O1b	0.5	-1.97	O1b	0.5	-2.05
	O2	1	-1.84	O2a	0.5	-2.26	O2a	0.5	-2.28
				O2b	0.5	-1.88	O2b	0.5	-2.31
2nd layer	Ti2	1	4.08	Ti2a	0.5	4.04	Ti2a	0.5	3.99
				Ti2b	0.5	4.02	Ti2b	0.5	3.97
	O3	1	-1.98	O3a	0.5	-2.17	O3a	0.5	-1.94
				O3b	0.5	-1.84	O3b	0.5	-1.87
	O4	1	-2.19	O4a	0.5	-2.31	O4a	0.5	-2.10
				O4b	0.5	-1.88	O4b	0.5	-2.05

The 2×2 reconstruction shows some undercoordination for most of its top layer atoms, but as its SII indicates (Table 4), the BVS numbers are clearly better than the high-energy 2×1 surface.

The following 0.5 ML structures (2 H₂O per 2×2 cell) were studied:

2×2 Mol: Molecular adsorption, where the H₂O molecules adsorb at Ti2, which is more undercoordinated than Ti1. A $p2gm$ symmetry constraint was imposed and upon relaxation the Ti–O bond tilts so as to favor a rough alignment of each O–H bond toward the nearby O1 at the surface, as seen in Fig. 4(b). This was a low-energy structure.

2×2 DissA: Dissociative adsorption. A hydroxyl group adsorbs at Ti2, with its O–H bond tilting toward one of the two neighboring O1. All such O–H bonds point toward the same direction. The corresponding lone H binds to the other O1 and this new O–H bond tilts so as to form an H-bond (1.87 Å) with an O3 from the next zigzag row of surface polyhedra. In this structure, the glide planes

are preserved, but not the 2-fold rotational symmetry. Its energy is slightly higher than that of 2×2 Mol, by a margin of $0.07 \text{ eV}/1 \times 1$. **2×2 DissB:** Dissociative adsorption. Similar to 2×2 DissA, except that (going along each zigzag) the adsorbed hydroxyl O–H bonds alternate orientations. Therefore, in this case the 2-fold rotational symmetry is preserved, while the glide planes are not. The energy of this model is higher than for the 2×2 Mol by $0.10 \text{ eV}/1 \times 1$.

The 2×2 Mol model, despite its relatively low energy, does not bring the Ti2 BVS dramatically closer to its optimal +4 value (Table 4); the same can be said for virtually every atom. While the bond valence metrics do get better, the improvement is modest, as evidenced by the comparable SII values.

In addition to the above, two full-monolayer structural models were tested:

2×2 SatD: Double dissociative adsorption. Every surface Ti acts as an adsorption site for hydroxyl groups. Each of the four lone H atoms binds to a surface O1 and this bond points toward an O3 from the next zigzag row of surface polyhedra so as to form H-bonds ($H3-O3 = 1.59 \text{ \AA}$; $H4-O3 = 1.63 \text{ \AA}$), as shown in Fig. 4(c). In this case, the 2-fold rotational symmetry is not preserved, but the glide planes are. In spite of this constraint and of being the only full-monolayer 2×2 structure studied, the energy of 2×2 Mol is the lowest of all the full-monolayer structural models.

2×2 SatM: Double molecular adsorption. This model is similar to 2×2 Mol, with an additional water molecule adsorbed on every Ti1. The original $p2gm$ is enforced. This adsorption configuration yields a surface energy $0.78 \text{ eV}/1 \times 1$ higher than the 2×2 SatD model.

The 2×2 SatD configuration succeeds in improving the bond-valence sums for almost every atom in the surface region, including the adsorbates. While there is some overcoordination of the O1-type atoms, it is comparable to the undercoordination exhibited in the lower H₂O coverage cases.

3.1.4. The $c(4 \times 2)$ surface

The $c(4 \times 2)$ structure was also solved by Erdman et al. [17], using the same methods as for the 2×1 . It exhibits $c2mm$ symmetry and a distinctive surface feature consisting of a clustered quartet of edge-sharing polyhedra, as shown in Fig. 5(a).

As Table 5 shows, the $c(4 \times 2)$ reconstruction shows both overcoordination (noticeably in O4, which sits at the center of the polyhedral quartet, bound to five Ti) as well as undercoordination (Ti1, Ti2

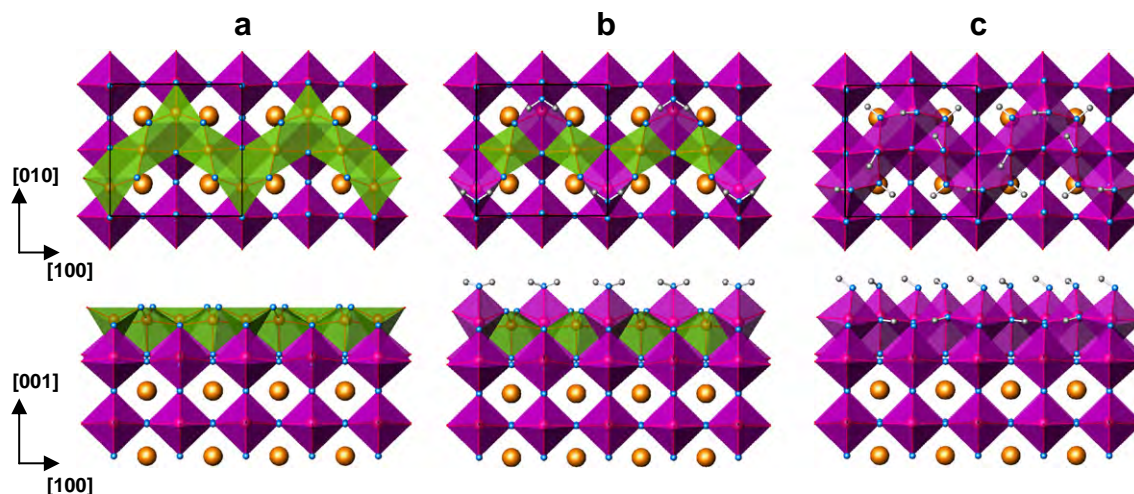


Fig. 4. Polyhedral representation of (a) the bare 2×2 surface, (b) the half-monolayer 2×2 Mol model, and (c) the full-monolayer 2×2 SatD model: plan view (top) and profile view (bottom). Surface cells outlined.

Table 4

Bond valence sums for the near-surface atoms of the 2×2 dry structure and low-energy hydrated models. The SII is also shown for each surface.

		2×2			2×2 Mol			2×2 SatD		
ML H ₂ O		0			0.5			1		
SII		0.17			0.15 (0.16)			0.10 (0.11)		
		Atom	m	BVS	Atom	m	BVS	Atom	m	BVS
Adsorbed atoms					O _w	0.5	-2.14	O _w 1	0.5	-1.88
					H1	1	0.97	H1	0.5	0.98
								H2	0.5	0.96
								O _w 2	0.5	-1.90
								H3	0.5	1.03
								H4	0.5	1.01
Top layer		Ti1	0.5	3.78	Ti1	0.5	3.86	Ti1	0.5	3.96
		Ti2	0.5	3.70	Ti2	0.5	3.72	Ti2	0.5	3.94
		O1	1	-1.83	O1	1	-1.81	O1a	0.5	-2.21
								O1b	0.5	-2.19
		O2	0.5	-2.09	O2	0.5	-2.05	O2	0.5	-2.04
		O3	0.5	-1.87	O3	0.5	-1.88	O3	0.5	-1.87
2nd layer		Ti3	0.5	3.88	Ti3	0.5	3.88	Ti3	0.5	3.99
		Ti4	0.5	4.16	Ti4	0.5	4.13	Ti4	0.5	3.90
		O4	0.5	-1.93	O4	0.5	-1.83	O4	0.5	-1.89
		O5	0.5	-2.06	O5	0.5	-2.12	O5	0.5	-1.87
		O6	0.5	-1.93	O6	0.5	-1.95	O6	0.5	-2.00
		O7	0.5	-2.24	O7	0.5	-2.21	O7	0.5	-2.11

and O1, which are the surface atoms surrounding O4) in its top layer. However, its SII is comparable to that of the 2×2 surface, much like their respective surface energies.

Two 0.5 ML models ($2 \text{ H}_2\text{O}$ per $c(4 \times 2)$ cell) were examined:

$c(4 \times 2)$ Mol: Molecular adsorption. Of the surface Ti atoms, the Ti2 are more undercoordinated than the Ti1 and, therefore, molecular water should preferentially adsorb on Ti2. The two H₂O groups of each polyhedral quartet tilt away from each other favoring the in-plane alignment of each O–H bond toward a surface O1, as shown in Fig. 5(b). The symmetry was constrained to $c2mm$.

$c(4 \times 2)$ Diss: Dissociative adsorption. One hydroxyl group adsorbs on each Ti2 atom. Each of these O–H bonds tilts slightly toward one of the nearby surface O1 atoms. A lone H binds to the other neighboring O1 and this new O–H bond aligns toward an O3 at the corner of a nearby polyhedral quartet, so as to form an H-bond (1.99 Å). Only the 2-fold rotational symmetry, not the mirror

planes, is preserved. The energy of this model is $0.08 \text{ eV}/1 \times 1$ higher than that of $c(4 \times 2)$ Mol.

Model $c(4 \times 2)$ Mol yields better BVS numbers than the dry case for the top-layer atoms (see Table 5), nudging them closer to their ideal values; however, it makes them worse for several atoms in the layer beneath. The net outcome is a slightly lower (yet certainly comparable) SII than for the bare surface.

Also, two full-monolayer structures were studied:

$c(4 \times 2)$ SatD: Double dissociative adsorption. Every surface Ti has a hydroxyl group adsorbed on it. While the O–H bonds above Ti1 point away from the center of the polyhedral quartet, the O–H bonds above Ti2 relax to point toward it. Every O1 atom has a lone H bound to it, with this new bond tilting toward an O3 from a nearby polyhedral quartet so as to form an H-bond (1.61 Å). See Fig. 5(c). This was found to be a low-energy structure.

$c(4 \times 2)$ SatM: Double molecular adsorption. Similar to $c(4 \times 2)$ Mol, with the addition of an adsorbed H₂O molecule on every Ti1, with all O–H pointing toward an O1 atom. The original $c2mm$ symmetry was preserved. This was found to have a surface energy $0.60 \text{ eV}/1 \times 1$ higher than $c(4 \times 2)$ SatD.

Model $c(4 \times 2)$ SatD has a lowest SII among the low-energy $c(4 \times 2)$ structures, as shown in Table 5. While a couple of top-layer O sites flip drastically from undercoordinated to overcoordinated (or vice versa), the overall shift is toward the ideal BVS values. The SII numbers for this periodicity, as well as the trend with varying water coverage, are similar to the 2×2 structures.

All twelve low-energy structures (i.e. those depicted in Figs. 2–5) are available as supplementary material in CIF format. The adsorption energies at 0 K for the low-energy wet structures are listed in Table 6. These correlate strongly with the change in SII with respect to the dry models, as shown in Fig. 6.

3.1.5. Thermodynamics

There are two main ways to look at the thermodynamics in question. The first is to examine the energetics as a function of the surface stoichiometry, keeping the chemical potential fixed (e.g. $T=0 \text{ K}$), while the second compares energies as a function of temperature. The items of interest in the first approach are the energies within each fixed water coverage, as well as the convex-hull construction;

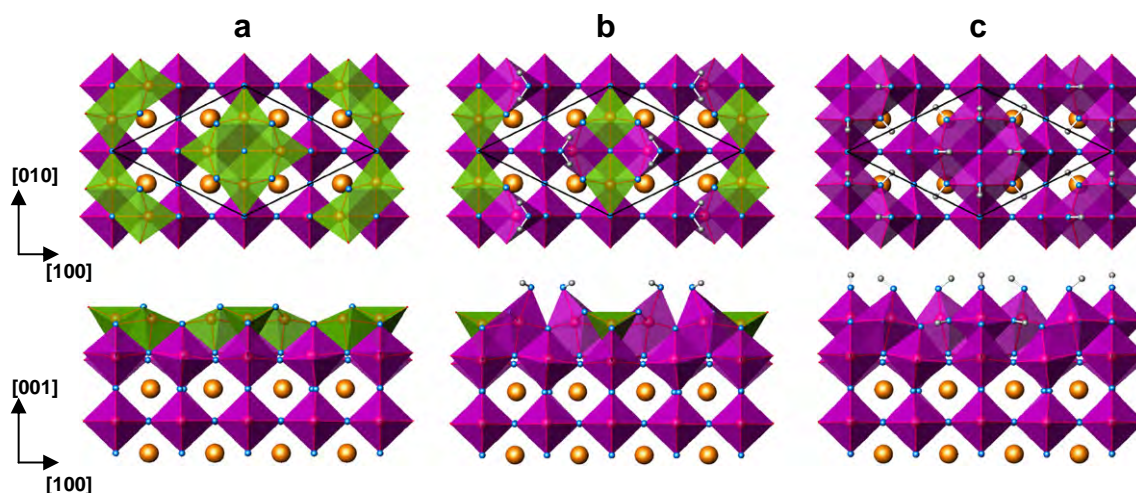


Fig. 5. Polyhedral representation of (a) the bare $c(4 \times 2)$ surface, (b) the half-monolayer $c(4 \times 2)$ Mol model, and (c) the full-monolayer $c(4 \times 2)$ SatD model: plan view (top) and profile view (bottom). Surface cells outlined.

Table 5
Bond valence sums for the near-surface atoms of the $c(4 \times 2)$ dry structure and low-energy hydrated models. The SII is also shown for each surface.

	$c(4 \times 2)$			$c(4 \times 2)$ Mol			$c(4 \times 2)$ SatD		
	Atom	<i>m</i>	BVS	Atom	<i>m</i>	BVS	Atom	<i>m</i>	BVS
ML H ₂ O	0			0.5			1		
SII	0.18			0.16 (0.17)			0.11 (0.13)		
Adsorbed atoms				O _w	0.5	-2.17	O _w 1	0.5	-1.91
				H1	1	0.97	H1	0.5	0.97
							O _w 2	0.5	-1.92
							H2	0.5	0.97
							H3	1	1.04
Top layer	Ti1	0.5	3.86	Ti1	0.5	3.93	Ti1	0.5	4.02
	Ti2	0.5	3.70	Ti2	0.5	3.75	Ti2	0.5	3.85
	O1	1	-1.81	O1	1	-1.78	O1	1	-2.20
	O2	0.25	-2.18	O2	0.25	-2.20	O2	0.25	-2.15
	O3	0.5	-1.89	O3	0.5	-1.92	O3	0.5	-1.94
	O4	0.25	-2.39	O4	0.25	-2.27	O4	0.25	-1.83
2nd layer	Ti3	0.25	4.20	Ti3	0.25	4.17	Ti3	0.25	3.91
	Ti4	0.5	3.96	Ti4	0.5	3.98	Ti4	0.5	4.02
	Ti5	0.25	4.23	Ti5	0.25	4.27	Ti5	0.25	4.06
	O5	0.5	-1.94	O5	0.5	-1.85	O5	0.5	-1.78
	O6	0.5	-2.06	O6	0.5	-2.13	O6	0.5	-1.93
	O7	0.5	-2.16	O7	0.5	-2.15	O7	0.5	-2.15
	O8	0.5	-1.95	O8	0.5	-1.96	O8	0.5	-1.98

the latter is most useful as errors in the energy of reference states (e.g. bulk SrTiO₃, TiO₂ and molecular H₂O) only rotate the convex hull and they do not change the predicted stable state for a given composition. As mentioned earlier, to first-order phonon entropy terms should cancel.

For this purpose, the surface energy was calculated for the lowest-energy structure for each water coverage and base periodicity. The revTPSSh values are plotted in Fig. 7, which largely resemble the trends of the SII numbers. The energies of the dry structures follow the same hierarchy as in the calculations by Warschkow et al. [18]. While the RT2 reconstruction definitely has the lowest energy among the bare structures, this is no longer clear-cut upon adsorption of H₂O. At half-monolayer coverage, all periodicities yield similar energies, nearly becoming degenerate; RT2Diss has the lowest calculated energy, but the difference with other periodicities is much smaller. At full-monolayer water adsorption, RT2SatD has a surface energy comparable to the 2×1 SatB and $c(4 \times 2)$ SatD configurations, with the 2×2 SatD as the most stable arrangement. A strict convex-hull construction skips all half-monolayer structures, and predicts the co-existence of RT2 and 2×2 SatD on the surface. The adsorption energies (Table 6) highlight that, even at full-monolayer coverage, the bare RT2 adsorbs H₂O more weakly than the other reconstructions and the bulk-like TiO₂ truncation (Table 1).

It is also clear that the 2×1 models follow an odd trend. Unlike the other periodicities, 0.5 ML adsorption is stronger than the full-monolayer case, which is consistent with the findings in Part I, where it was shown that the 2×1 DissA model more adequately reproduces the STM images than the bare structure. Of all the dry DL

Table 6
Predicted drying temperature, adsorption energies and solid angle (with respect to first adsorption Ti site) subtended by four surrounding surface O, for different DL periodicities.

	E_{ads} (eV/H ₂ O)		Ti–O ₄ solid angle (π sr)	T_{dry} (°C)
	0.5 ML	1 ML		
2×1	2.16	1.63	2.16	769
RT2	0.41	0.64	1.63	240
2×2	0.80	1.13	1.67	420
$c(4 \times 2)$	0.52	0.96	1.66	360

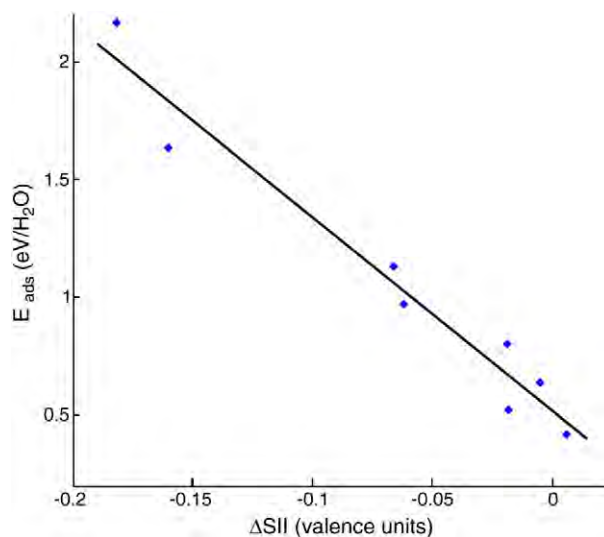


Fig. 6. Adsorption energies as a function of change in the surface instability index ($\Delta\text{SII} = \text{SII}_{\text{wet}} - \text{SII}_{\text{dry}}$). The linear fit has an R^2 coefficient of 0.95.

reconstructions, only the 2×1 has a surface Ti site (Ti2) where the position of every neighboring O is heavily constrained, inhibiting any significant bond shortening or outward relaxation. The environment around Ti2 is thus similar to octahedral Ti sites in the bulk, but with only 5 surrounding oxygen atoms, rendering it an ideal site for adsorption. This atom is also very exposed, which makes it easy for foreign molecules to approach it, as compared to the more concealed surface Ti elsewhere; Table 6 lists the solid angle subtended by the four neighboring top-layer O with respect to the worst-BVS Ti in each bare structure. Adsorption on the dry 2×1 is further enhanced by the severely undercoordinated “dangling” oxygen (O1), an ideal site for H from dissociated water.

The second approach uses the temperature as the main variable. Fig. 8 shows the energy of all twelve structures as a function of temperature, upon correction due to the chemical potential of water; we note that this assumes that the surface is in full equilibrium with the water vapor. A similar story is found here, as the 2×2 SatD has the lowest surface energy up to 334 °C, above which it is the bare RT2 that is the most stable. Within each periodicity, this method allows us to predict transition temperatures (ignoring any inherent

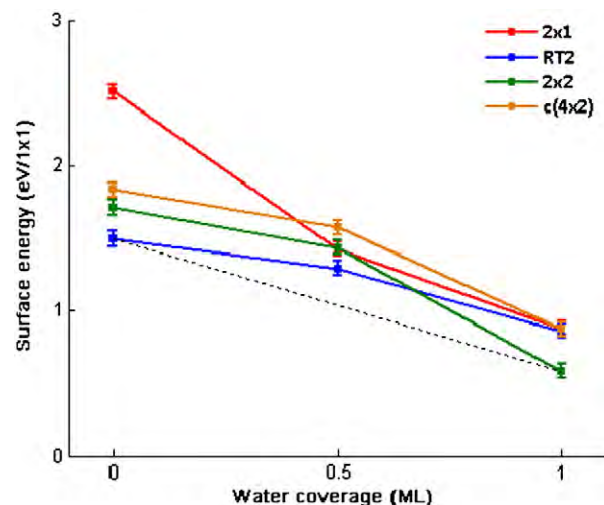


Fig. 7. Normalized revTPSSh surface energies for low-energy structures, pictured in Figs. 2–5. Convex-hull construction is shown with the dotted black line.

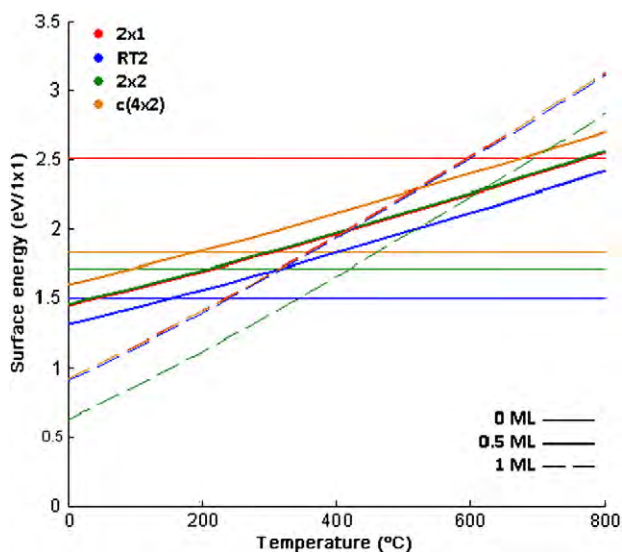


Fig. 8. Surface energies for low-energy structures as a function of temperature.

activation energy). Table 6 lists the temperatures above which the dry surface becomes more stable than its “wet” counterparts; it is no coincidence that this metric follows the same trend as the solid angle discussed above. It is worth remarking that for the RT2, 2×2 and $c(4 \times 2)$ periodicities, the half-monolayer structure is never predicted to be favored. On the other hand, 2×1 DissA has the lowest 2×1 -periodicity energy in the 410–769 °C range; this is associated to the sharp energy drop mentioned above. All full-monolayer structures are stable at low temperatures, including room temperature.

3.1.6. The $c(4 \times 4)$ surface

It is appropriate to include here the total energy calculations of the 2×1 -based $c(4 \times 4)$ model presented in Part I [38]. Briefly, a model was constructed which has the same base structure as the dry 2×1 structure, as well as 0.25 ML water coverage, following the favorable adsorption sites found from the 0.5 ML 2×1 DissA structure. DFT-based scanning tunneling micrograph (STM) simulations were consistent with experiment, which is highly suggestive of a simple dehydration process to explain the 2×1 -to- $c(4 \times 4)$ transition upon annealing.

Energetically, the $c(4 \times 4)$ A model is slightly lower in energy than a combination of structures of 2×1 periodicities:

$$\Delta H \left[\frac{1}{2} [(2 \times 1) + (2 \times 1 \text{ DissA})] \rightarrow c(4 \times 4) \text{A} \right] = -0.04 \text{ eV}/1 \times 1.$$

Moreover, the alternative model discarded due to its poor STM simulation, $c(4 \times 4)$ B, was calculated to be a little higher in energy (0.03 eV/ 1×1). All these energies are within error, but this highlights that the $c(4 \times 4)$ A model is certainly energetically reasonable.

3.2. Experimental

Multiple samples were annealed, and the following reconstructions were observed: 2×1 , $c(4 \times 2)$ and $(\sqrt{13} \times \sqrt{13})R33.7^\circ$. The latter will not be analyzed here, since the dry structure [39] is less Ti-rich than the DL structures.

3.2.1. The $c(4 \times 2)$ surface

A sample annealed at 950 °C for 5 h in air showed a clear $c(4 \times 2)$ electron diffraction pattern, as shown in Fig. 9. The XPS spectrum showed a high binding energy shoulder on the O-1s peak, with an area 0.36 times the area of the main peak, as shown in Fig. 10(a).

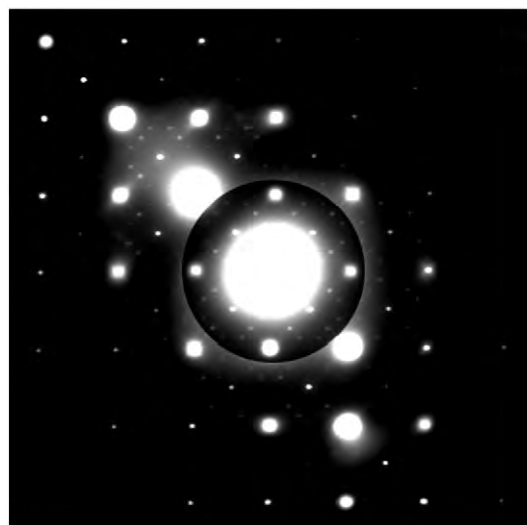


Fig. 9. $c(4 \times 2)$ electron diffraction pattern after an anneal in air at 950 °C for 5 h.

There is a third feature that is attributed to differential charging between the sample and the holder, addressed in Ref. [14]. The C-1s region also showed a peak, with an area (also relative to the O-1s peak) of 0.34.

This specimen was next annealed at 400 °C for 20 min with the electron gun, at an O_2 partial pressure of 8×10^{-7} Torr. This resulted in a slightly weaker $c(4 \times 2)$ pattern. However, this does not necessarily imply a structural change; a difference in the tilt condition or the sample thickness with respect to the air-annealed sample could be responsible. The O-1s shoulder had a relative area of 0.55 (Fig. 10(b)) and the C-1s peak was slightly smaller, at 0.30.

A longer, 3 h electron-gun anneal at 300 °C in 4×10^{-6} Torr of O_2 had little effect on the diffraction pattern and intensities. Nonetheless, the O-1s shoulder did drop to a relative area of 0.08, as shown in Fig. 10(c), while the C-1s peak was also lowered to 0.15. The Ti-2p region showed a pair of extra peaks, corresponding to the reduction of Ti (Ti^{3+}). The Ti^{3+} area, relative to Ti^{4+} , was 0.67 at a 45° collection angle, but 0.60 at 60°, indicating that most reduction occurs at the surface. Since Ti^{3+} also contributes to the high binding energy O-1s shoulder, the shoulder area attributable to hydroxylation is thus smaller than the already small measured value. Few if any hydroxyl groups remain.

A final electron-gun anneal at 800 °C for 20 min at 9×10^{-7} Torr of O_2 made the reconstruction nearly disappear (not shown). The O-1s shoulder did not change much, this time with a relative area of 0.07 (see Fig. 10(d)), while the C-1s peak had an area of 0.18. The Ti-2p $3+ : 4+$ area ratio shrank to 0.26 at 45° collection angle and 0.46 at 60°; this suggests that most of the reduction lies deeper into the sample than before this anneal. However, it must be emphasized that for this high temperature the electron beam has to be focused onto a small area of the sample, so the heating is not homogeneous. Therefore, barring a perfect alignment, it is likely that different regions of the sample were probed at different tilts (the sample itself is tilted, not the detector), so the angle-dependent Ti-2p results should not be overinterpreted. Lower-temperature anneals do not share this problem, as the beam is much broader.

3.2.2. The 2×1 surface

A different specimen, also annealed at 950 °C for 5 h in air, exhibited a weak 2×1 TED pattern, with streaks along the $\{100\}$ -type directions, which partially resolve into a 5×1 periodicity (Fig. 11). The XPS spectrum showed a O-1s shoulder, with higher binding energy than the main peak, and a relative area of 0.19. The C-1s area also

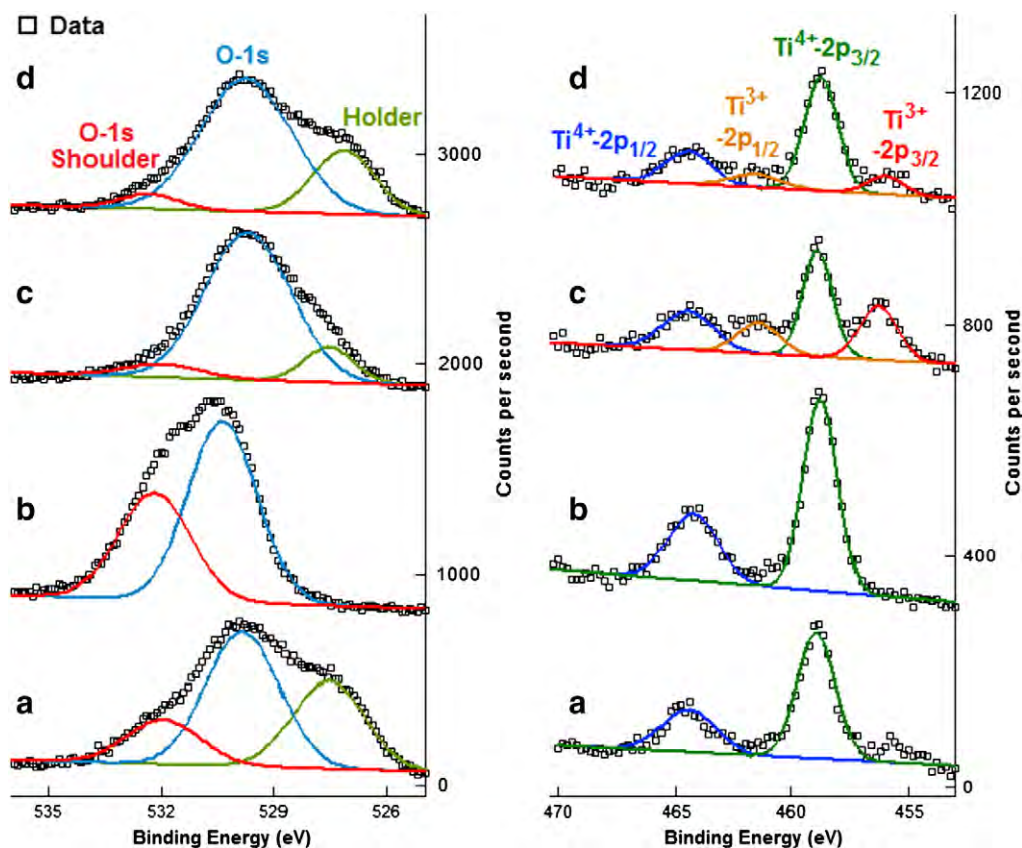


Fig. 10. O-1s (left) and Ti-2p (right) XPS peak regions from a sample with the $c(4 \times 2)$ reconstruction. Counts per second for each spectrum offset for ease of viewing. After: (a) air anneal for 5 h at 950 °C, (b) anneal in 8×10^{-7} Torr O_2 for 20 min at 400 °C, (c) anneal in 4×10^{-6} Torr O_2 for 3 h at 300 °C, and (d) anneal in 9×10^{-7} Torr O_2 for 20 min at 800 °C.

showed a peak with an area of 0.29, relative to the O-1s peak. All relevant XPS spectra are shown in Fig. 12.

The sample was then annealed at 750 °C for 5 h in 2×10^{-2} Torr of O_2 . The streaks and incipient 5×1 periodicity disappeared from the diffraction pattern, and the 2×1 reflections were stronger; see Fig. 13. The XPS O-1s shoulder had a relative area of 0.11 and no discernible C-1s (nor Ti^{3+}) signal was found.

This specimen was exposed to air for 1 h before being re-inserted into the UHV system. The XPS spectrum shows no C-1s peak,

indicating no adsorption of CO_2 or other carbonaceous contaminants. The O-1s high binding energy shoulder grew to a relative area of 0.18. No TED analysis was performed, as the sample was lost while being transported.

4. Discussion

The theoretical modeling of water adsorption configurations on periodic $SrTiO_3(001)$ surface reconstructions yields new insights into the factors governing the preferential formation of some structures over others. It becomes apparent, for example, that the RT2 reconstruction is kinetically inaccessible and that the inescapable interaction of the surface with environmental water vapor favors other configurations. This finding is similar to the case of the low-energy Wolf octapole $MgO(111)$ structure, which has not been experimentally observed either; Ciston et al. [14] showed that the high surface mobility of hydrogen atoms, with respect to the slow cationic diffusion, favors the formation of other structures.

It is important to recognize that as-prepared surfaces will invariably start with some amount of chemisorbed water. In the particular case of $SrTiO_3$ crystals, no preparation method yields perfectly flat surfaces. For specimens to be analyzed by TEM/TED or by scanning probe microscopies, the sample preparation steps typically include ion bombardment and/or chemical etching with aqueous solutions. In either case, surface defects (point defects or step edges) will act as strong adsorption sites for environmental water, mostly in a dissociative fashion [6–8]; even cleaving $SrTiO_3$ crystals in UHV will generate surface vacancies [40]. Subsequent annealing steps will induce a competition between desorption of the water and ordering of the surface to stabilize it. As long as the surface is not fully ordered, defect sites (and thus strong H_2O adsorption sites) will remain. Therefore, it is not the thermodynamics of bare surface reconstructions that

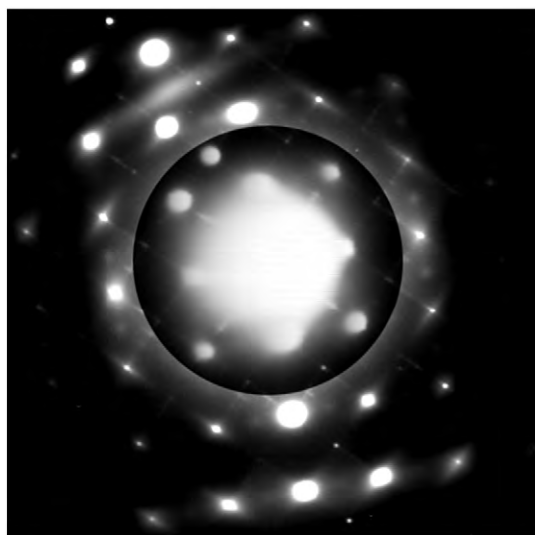


Fig. 11. (2×1) electron diffraction pattern with streaks in the (100) directions nearly resolving into a (5×1) reconstruction, from a sample annealed in air at 950 °C for 5 h.

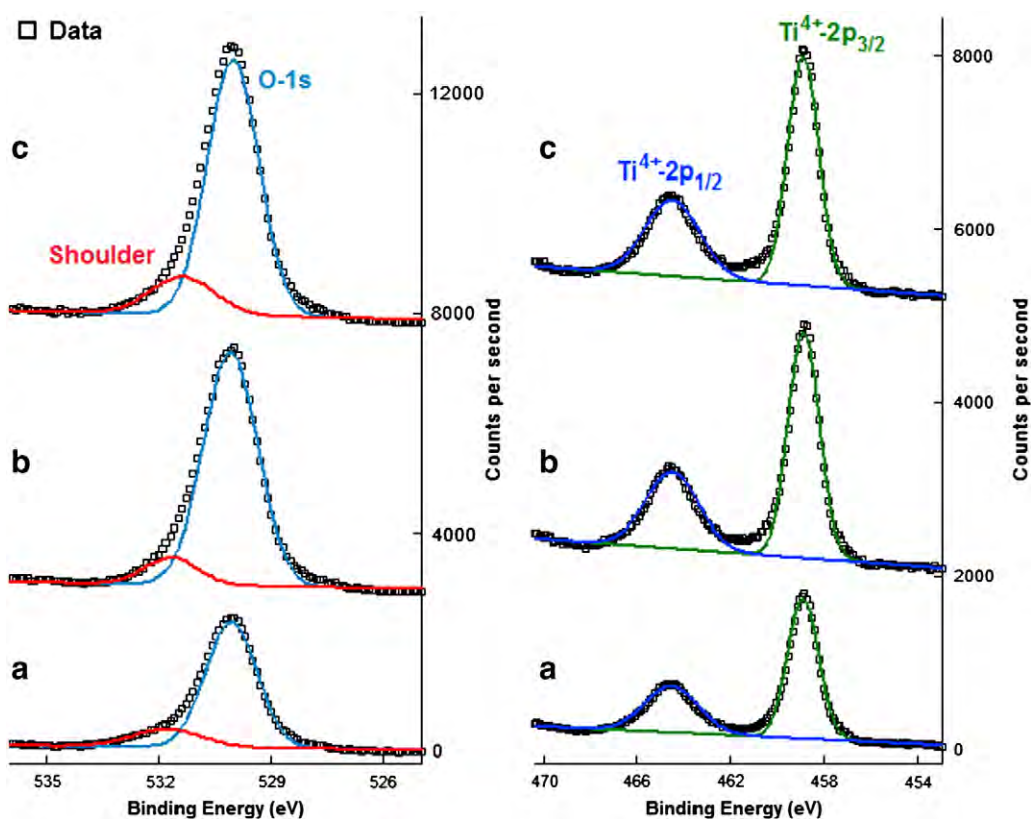


Fig. 12. O-1s (left) and Ti-2p (right) XPS peak regions of a sample which began with the (2×1) reconstruction. Counts per second for each spectrum offset for ease of viewing. After: (a) air anneal for 5 h at 950 °C, (b) anneal in 2×10^{-2} Torr O_2 for 5 h at 750 °C, and (c) exposure to air.

govern the stabilization process; it is the “wet” kinetics that do. The easy diffusion of oxygen and (especially) hydrogen will dominate over the slow rearrangement of surface Ti; that the 2×1 sample required further treatment to fully order is a clear example of the sluggish cation diffusion. Ultimately, the local inhomogeneities developed during the processing stages will determine which particular structure forms, with the coexistence of multiple reconstructions as a distinct possibility.

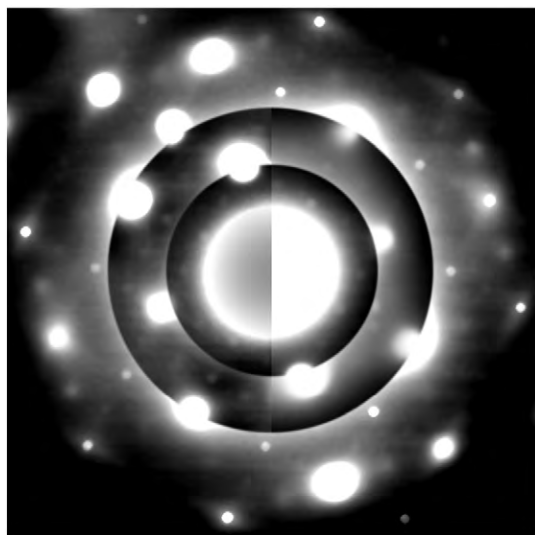


Fig. 13. (2×1) electron diffraction pattern following anneal at 750 °C in 2×10^{-2} Torr O_2 . High-pass filter applied to left half of image to enhance visibility of (2×1) diffraction spots.

Furthermore, other predictions can be drawn from our computational results:

- 1) Water favorably adsorbs on all $SrTiO_3(001)$ DL reconstructions at ambient temperature and pressure;
- 2) On the 2×1 reconstruction, the strongest H_2O adsorption occurs at half-monolayer coverage, in agreement with the results of Part I, which strongly suggest that the 2×1 DissA model is a more accurate description than its dry counterpart;
- 3) Moreover, the 2×1 -based hydrated model (0.25 ML) of the $c(4 \times 4)$ reconstruction, introduced in the companion paper, is further supported by the total energy calculations described here;
- 4) Hydrogen bonding plays a significant role in the stabilization of most hydrated surfaces, especially upon dissociative water adsorption and often bridging surface polyhedra.

On the experimental front, the XPS spectra presented herein are consistent with our prediction that water on the $c(4 \times 2)$ reconstruction should desorb much more easily (at a much lower temperature) than on the 2×1 . Also, they demonstrate that a dry $c(4 \times 2)$ -reconstructed surface can indeed be attained.

More generally, it is imperative to stress that adsorbates (such as H_2O) on an oxide surface can no longer be assumed to be absent or irrelevant. Not only are they likely to be present, even at high temperatures and in ultra high vacuum, but they also play an important role in the formation of stable surface structures.

5. Conclusions

We have explored a wide variety of H_2O adsorption configurations on reconstructed $SrTiO_3(001)$ surfaces via DFT, which elucidate the factors favoring the formation of certain structures. For example, the dry surface thermodynamics predict the RT2 reconstruction to be much more stable than the 2×1 , yet the former has never been

detected and the latter repeatedly has. Accounting for the interaction with water molecules leads to surface energies which are much more consistent with the experimental observations; at full-monolayer adsorption, the RT2 periodicity is no longer the most favorable. Therefore, it is the kinetics that rule over the simplistic dry-surface thermodynamics by favoring ordering with other periodicities.

Acknowledgments

We thank Prof. K.R. Poepplmeier for useful discussions. The theoretical portion of this research was supported by the U.S. Department of Energy, under award number DE-FG02-01ER45945. The experimental portion of this research was supported by the Northwestern University Institute for Catalysis in Energy Processing, funded through the U.S. Department of Energy, Office of Basic Energy Science, under award number DE-FG02-03-ER15457. The authors acknowledge that the research reported in this study was in part performed on Quest, Northwestern University's centrally provided high performance computing facility, which is operated by Northwestern University Information Technology. Use of the Carbon Cluster at the Center for Nanoscale Materials was supported by the U.S. Department of Energy, Office of Science, Office of Basic Energy Sciences, under award number DE-AC02-06CH11357.

Appendix A. Supplementary data

Supplementary data to this article can be found online at [doi:10.1016/j.susc.2012.01.010](https://doi.org/10.1016/j.susc.2012.01.010).

References

- [1] M.S. Wrighton, A.B. Ellis, P.T. Wolczanski, D.L. Morse, H.B. Abrahamson, D.S. Ginley, *J. Am. Chem. Soc.* 98 (1976) 2774.
- [2] T. Puangpetch, T. Sreethawong, S. Yoshikawa, S. Chavadej, *J. Mol. Catal. A Chem.* 312 (2009) 97.
- [3] D.C. Johnson, A.L. Prieto, *J. Power Sources* 196 (2011) 7736.
- [4] J.A. Enterkin, W. Setthapun, J.W. Elam, S.T. Christensen, F.A. Rabuffetti, L.D. Marks, P.C. Stair, K.R. Poepplmeier, C.L. Marshall, *ACS Catal.* 1 (2011) 629.
- [5] J.A. Enterkin, K.R. Poepplmeier, L.D. Marks, *Nano Lett.* 11 (2011) 993.
- [6] L.-Q. Wang, K.F. Ferris, G.S. Herman, *J. Vac. Sci. Technol., A* 20 (2002) 239.
- [7] S. Eriksen, P.D. Naylor, R.G. Egdell, *Spectrochim. Acta A* 43 (1987) 1535.
- [8] N.B. Brookes, F.M. Quinn, G. Thornton, *Vacuum* 38 (1988) 405.
- [9] L.-Q. Wang, K.F. Ferris, S. Azad, M.H. Engelhard, *J. Phys. Chem. B* 109 (2005) 4507.
- [10] R.A. Evarestov, A.V. Bandura, V.E. Alexandrov, *Surf. Sci.* 601 (2007) 1844.
- [11] B.B. Hinojosa, T. Van Cleve, A. Asthagiri, *Mol. Simul.* 36 (2010) 604.
- [12] J. Ciston, A. Subramanian, D.M. Kienzle, L.D. Marks, *Surf. Sci.* 604 (2010) 155.
- [13] C. Di Valentin, A. Tilocca, A. Selloni, T.J. Beck, A. Klust, M. Batzill, Y. Losovsky, U. Diebold, *J. Am. Chem. Soc.* 127 (2005) 9895.
- [14] J. Ciston, A. Subramanian, L.D. Marks, *Phys. Rev. B* 79 (2009) 085421.
- [15] N. Erdman, K.R. Poepplmeier, M. Asta, O. Warschkow, D.R. Ellis, L.D. Marks, *Nature* 419 (2002) 55.
- [16] R. Herger, P.R. Willmott, O. Bunk, C.M. Schlepütz, B.D. Patterson, *Phys. Rev. Lett.* 98 (2007) 076102.
- [17] N. Erdman, O. Warschkow, M. Asta, K.R. Poepplmeier, D.R. Ellis, L.D. Marks, *J. Am. Chem. Soc.* 125 (2003) 10050.
- [18] O. Warschkow, M. Asta, N. Erdman, K.R. Poepplmeier, D.E. Ellis, L.D. Marks, *Surf. Sci.* 573 (2004) 446.
- [19] P. Blaha, K. Schwarz, G.K.H. Madsen, D. Kvasnicka, J. Luitz, WIEN2k, An Augmented Plane Wave + Local Orbitals Program for Calculating Crystal Properties, Universität Wien, Austria, , 2010.
- [20] J.P. Perdew, A. Ruzsinszky, G.I. Csonka, O.A. Vydrov, G.E. Scuseria, L.A. Constantin, X. Zhou, K. Burke, *Phys. Rev. Lett.* 100 (2008) 136406.
- [21] L.D. Marks, A.N. Chiaramonti, F. Tran, P. Blaha, *Surf. Sci.* 603 (2009) 2179.
- [22] A. Stroppa, G. Kresse, *New J. Phys.* 10 (2008).
- [23] J.P. Perdew, A. Ruzsinszky, G.I. Csonka, L.A. Constantin, J. Sun, *Phys. Rev. Lett.* 103 (2009) 026403.
- [24] M.W. Chase, NIST-JANAF Thermochemical Tables, 4th ed. American Chemical Society, Washington, D.C., 1998.
- [25] O. Warschkow, Y. Wang, A. Subramanian, M. Asta, L.D. Marks, *Phys. Rev. Lett.* 100 (2008) 086102.
- [26] I.D. Brown, D. Altermatt, *Acta Crystallogr., Sect. B: Struct. Sci.* 41 (1985) 244.
- [27] W.S. Benedict, N. Gailar, E.K. Plyler, *J. Chem. Phys.* 24 (1956) 1139.
- [28] K. Knížek, Kalvados, <http://www.fzu.cz/~knizek/kalvados/index.html>.
- [29] A. Salinas-Sanchez, J.L. Garcia-Muñoz, J. Rodriguez-Carvajal, R. Saez-Puche, J.L. Martinez, *J. Solid State Chem.* 100 (1992) 201.
- [30] I.D. Brown, *Acta Crystallogr., Sect. B: Struct. Sci.* 48 (1992) 553.
- [31] J.A. Enterkin, A.E. Becerra-Toledo, K.R. Poepplmeier, L.D. Marks, *Surf. Sci.* 606 (2012) 344.
- [32] N. Erdman, L.D. Marks, *Surf. Sci.* 526 (2003) 107.
- [33] V.K. Lazarov, R. Plass, H.C. Poon, D.K. Saldin, M. Weinert, S.A. Chambers, M. Gajdardziska-Josifovska, *Phys. Rev. B* 71 (2005).
- [34] S. Yamamoto, H. Bluhm, K. Andersson, G. Ketteler, H. Ogasawara, M. Salmeron, A. Nilsson, *J. Phys. Condens. Matter* 20 (2008) 184025.
- [35] H. Bluhm, *J. Electron Spectrosc.* 177 (2010) 71.
- [36] S.W. Knipe, J.R. Mycroft, A.R. Pratt, H.W. Nesbitt, G.M. Bancroft, *Geochim. Cosmochim. Acta* 59 (1995) 1079.
- [37] L.-Q. Wang, D.R. Baer, M.H. Engelhard, *Surf. Sci.* 320 (1994) 295.
- [38] A.E. Becerra-Toledo, M.R. Castell, L.D. Marks, *Surf. Sci.* xxx (2012) xxx.
- [39] D.M. Kienzle, A.E. Becerra-Toledo, L.D. Marks, *Phys. Rev. Lett.* 106 (2011) 176102.
- [40] A.F. Santander-Syro, O. Copie, T. Kondo, F. Fortuna, S. Pailhes, R. Weht, X.G. Qiu, F. Bertran, A. Nicolaou, A. Taleb-Ibrahimi, P. Le Fevre, G. Herranz, M. Bibes, N. Reyren, Y. Apertet, P. Lecoeur, A. Barthelemy, M.J. Rozenberg, *Nature* 469 (2011) 189.